

Contents lists available at ScienceDirect

### Chemical Engineering Journal

journal homepage: www.elsevier.com/locate/cej





## Atomically dispersed ruthenium in carbon aerogels as effective catalysts for pH-universal hydrogen evolution reaction

Ting He<sup>a,b</sup>, Yaya Song<sup>a</sup>, Yang Chen<sup>a</sup>, Xianwen Song<sup>a</sup>, Bingzhang Lu<sup>c</sup>, Qiming Liu<sup>c</sup>, Hongtao Liu<sup>a</sup>, Yi Zhang<sup>a,d,\*</sup>, Xiaoping Ouyang<sup>b,\*</sup>, Shaowei Chen<sup>c,\*</sup>

- <sup>a</sup> Hunan Provincial Key Laboratory of Micro & Nano Materials Interface Science, College of Chemistry and Chemical Engineering, Central South University, Changsha 410083, China
- <sup>b</sup> School of Materials Science and Engineering, Xiangtan University, Xiangtan 411105, China
- <sup>c</sup> Department of Chemistry and Biochemistry, University of California, 1156 High Street, Santa Cruz, CA 95064, United States
- d Key Laboratory of Materials Processing and Mold (Zhengzhou University), Ministry of Education, Zhengzhou 450002, China

#### ARTICLE INFO

# Keywords: Atomically dispersed ruthenium Carbon aerogel Hydrogen evolution reaction Water splitting pH-universal catalyst

#### ABSTRACT

Development of cost-effective catalysts for hydrogen evolution reaction (HER) plays a significant role in scalable production of hydrogen. Herein, carbon aerogels doped with atomically isolated Ru are produced pyrolytically from biomass hydrogels and exhibit a remarkable performance in HER within a broad range of solution pH, due to the formation of abundant RuN<sub>x</sub> moieties. At the current density of 10 mA cm $^{-2}$ , the optimal sample (NCAG/Ru-3) exhibits an ultralow overpotential of merely -4 mV in 1.0 M KOH, -45 mV in 1.0 M phosphate buffer solution and -65 mV in 0.5 M H<sub>2</sub>SO<sub>4</sub>, with the respective mass activity 44, 16 and 6 times that of commercial Pt/C benchmark. The excellent performance is also manifested in full water splitting. Theoretical calculations suggest that the high activity arise from the RuN<sub>x</sub> sites at the zigzag edges and nanowrinkles. These results underscore the unique quality of carbon aerogel-based single atom catalysts in electrochemical energy technologies.

#### 1. Introduction

Platinum (Pt)-based nanomaterials have been the catalysts of choice for hydrogen evolution reaction (HER) [1-6], a critical process in hydrogen production from water splitting [7,8]. However, the widespread application of the technology has been severely hampered by the high cost and limited natural reserve of Pt. Thus, there is an urgent need to develop cost-effective HER catalysts, and ruthenium (Ru) has emerged as an attractive candidate, largely because of a moderate strength of the ruthenium-hydrogen (Ru-H) bond that is analogous to that of Pt-H, which is conducive to facile HER kinetics [9-18]. In addition, Ru is under 5% the cost of Pt [19,20]. However, the natural reserve of Ru is relatively scarce, thus it is of great significance to maximize the mass activity of Ru-based HER catalysts, which involves two leading strategies. The first is to improve the atom utilization efficiency of Ru by reducing the size and alloying of Ru nanoparticles [21–32]; and the other is to enhance the intrinsic activity of the metal sites [30,33-41]. Among these, Ru atomically dispersed within a carbon matrix represents a unique system, with an HER performance markedly

better than the nanoparticle counterparts [20,42]. Within this context, enhancement of the atomic dispersion of Ru and stabilization of the single atom moieties are critical in maximizing the HER performance.

Carbon aerogels are a three-dimensional (3D) material with rich porosity and nanowrinkles [43–46], where spatial confinement by the abundant micropores and nanowrinkles of the carbon aerogels facilitates the incorporation of isolated metal atoms. More importantly, the single metal atom sites at the micropores and nanowrinkles often entail an asymmetrical coordination shell, as compared to single atom sites on a basal plane [44,47]. This structural asymmetry may impact the electron density and distribution of the metal atoms and adjacent atoms, leading to an increase of the intrinsic activity of the atomic sites. With these two advantages in mind, one can infer that doping Ru sites into a carbon aerogel can produce atomically dispersed Ru catalysts with high mass activity by improving both the "quantity" and "quality" of the active sites.

In the present study, a biomass hydrogel was used as the structural template to produce carbon aerogels embedded with  $RuN_x$  atomic sites and Ru nanoclusters [43]. The loading of atomically dispersed Ru in the

E-mail addresses: yzhangcsu@csu.edu.cn (Y. Zhang), oyxp2003@aliyun.com (X. Ouyang), shaowei@ucsc.edu (S. Chen).

<sup>\*</sup> Corresponding authors.

nanocomposite was varied from 43% to 86% by regulating the initial feed ratio of the hydrogel precursors and the metal salts, as manifested in microscopic and spectroscopic measurements. Results from first principles calculations show that the produced  $RuN_x$  sites accelerated  $H_2O$  dissociation, promoted H absorption/desorption, and acted as promising active sites for HER. Electrochemically, the obtained carbon aerogels indeed exhibited a remarkable HER activity across a wide pH range of 0 to 14. The optimal sample possessed the highest concentration of  $RuN_x$  and hence markedly outperformed commercial Pt/C in neutral and alkaline media, and the performance was only slightly subpar in acidic media. In overall water splitting, this sample also showed a low cell voltage and superb longtime stability, as compared to the commercial benchmark, indicating that the aerogel nanocomposites can be used as effective, pH-universal HER catalysts for full water splitting.

#### 2. Experimental section

#### 2.1. Preparation of NCAG/Ru nanocomposites.

The chemicals used in the present study were all of analytical grade and detailed in the Supplementary Information. In a typical experiment, gelatin (120 mg),  $SiO_2$  (100 mg), and MilliQ water (5.0 mL) were mixed under magnetic stirring in a water bath (60 °C), into which were then added 0.05 M RuCl $_3$  (200  $\mu L$ ), 1,10-phenanthroline monohydrate (PM, 17.8 mg) and 1.0 M zinc acetate (160  $\mu L$ ). After three freezing-thawing cycles, a hydrogel was produced (denoted as  $G_{Si}/Ru\text{-PM}$ ), which was then converted into carbon aerogels (NCAG/Ru-3) by freeze-drying, pyrolysis at 900 °C for 3 h (97% Ar + 3% H $_2$ ) and etching with 3 wt% HF.

Two additional samples, NCAG/Ru-1 or NCAG/Ru-2, were fabricated in the same fashion but with the addition of 0 or 3 mg PM, respectively. Metal-free NCAG was also fabricated in the same manner of NCAG/Ru-3 except for the addition of  $RuCl_3$ .

Experimental details of sample structural characterizations are included in the Supplementary Information.

#### 2.2. Electrochemical studies

Electrochemical measurements were all performed in a threeelectrode cell, including a glassy carbon working electrode, a KClsaturated Ag/AgCl reference electrode and a graphite rod counter electrode. Catalyst inks were prepared by dispersing the carbon aerogels (2 mg) produced above into a mixture of water and ethanol (v:v = 1:1. 475 μL in total) and Nafion solution (5%, 25 μL). A calculated amount of the catalyst inks was then dropcast onto the glassy carbon electrode surface at a mass loading of 0.4 mg cm<sup>-2</sup>. Electrochemical data were acquired at 90% IR-compensation. The calibration of the KCl-saturated Ag/AgCl reference electrode against the reversible hydrogen electrode (RHE) was performed in a high-purity H<sub>2</sub> saturated electrolyte with a Pt wire as the working electrode and counter electrode (Fig. S1). The average open-circuit voltage was taken as the thermodynamic potential of the hydrogen electrode reaction. In 1.0 M KOH,  $E_{Ag/AgCl} = E_{RHE} +$ 1.035 V; in 0.5 M  $H_2SO_4,\,E_{Ag/AgCl}=E_{RHE}+0.235$  V; and in 1.0 M PBS,  $E_{\text{Ag/AgCl}} = E_{\text{RHE}} + 0.617 \text{ V.} \label{eq:energy}$ 

For overall water splitting, commercial RuO<sub>2</sub> was employed as the anode catalyst and the carbon aerogels prepared above or commercial 20 wt% Pt/C as the cathode catalyst. The electrode for water splitting was composed of a Ni foam (or carbon paper) layer and a catalyst layer. The latter was prepared by adopting the method reported previously [9].

#### 2.3. Theoretical calculations

All calculations were conducted with the Vienna ab initio Simulation Package (VASP) [48–51]. Additional details can be found in the Supplementary Information.

#### 3. Results and discussion

#### 3.1. Sample synthesis and structural characterization

The synthetic procedure of the carbon aerogels is schematically illustrated in Fig. S2, where a gelatin-zinc hydrogel (Gsi/Ru-PM) was employed as the structural template, SiO<sub>2</sub> nanoparticles as the porogen and a ruthenium-phenanthroline (Ru-PM) complex as the metal and nitrogen sources. Scanning electron microscopy (SEM) measurements show that the freeze-dried GSi/Ru-PM hydrogel exhibited a 3D porous network (Fig. 1a and S3a), and was readily transformed into highly porous carbon aerogels doped with Ru individual atoms and nanoclusters after pyrolysis at a controlled temperature and HF etching to remove SiO<sub>2</sub>, as manifested in SEM (Figure S3b) and transmission electron microscopy (TEM) measurements [44]. Notably, the Ru morphological structures can be readily manipulated by the molar feed ratio (n) of PM to Ru in the hydrogel precursors. From the TEM images in Fig. S4, it can be observed that in the absence of PM (n = 0), the resultant carbon aerogels contained a number of metal nanoclusters of about 2 nm in diameter (NCAG/Ru-1, Fig. S4a); yet at n = 1.5, the number of nanoclusters in the carbon aerogel (NCAG/Ru-2) diminished markedly by half, along with a reduced size of about 1 nm in diameter (Fig. S4b). With a further increase of the PM feed (n = 9), the resulting carbon aerogel (NCAG/Ru-3) contained only a handful of nanoclusters with an even smaller size (Fig. 1b), and well-defined lattice fringes can be resolved in high-resolution TEM imaging of the metal nanocluster (Fig. 1b inset) with an interplanar d-spacing of 2.05 Å, which is consistent with the (101) facet of hcp Ru (PDF #65-7646). Additionally, high-angle annular dark-field scanning TEM (HAADF-STEM) measurements showed that the sample actually contained a large number of single metal atoms within the porous carbon aerogel (Fig. 1c). Elemental mapping analysis showed that both N and Ru were scattered rather evenly across the C scaffold of the sample, without significant agglomeration, confirming successful doping of these elements into the nanocomposites (Fig. 1d).

Interestingly, in spite of the different numbers of nanoclusters in the three samples, the total Ru content was actually very close at ca. 0.47 wt % (Table S1), as determined by inductively coupled plasma-optical emission spectrometry (ICP-OES) measurements. This suggests a different partition of Ru between single atoms and nanoclusters in the sample series. That is, an increasing PM feed facilitated the formation of Ru single atoms, with the fraction varying in the order of NCAG/Ru-1 < NCAG/Ru-2 < NCAG/Ru-3.

Further structural insights of these carbon aerogels were investigated by N2 absorption-desorption isotherms and X-ray diffraction (XRD) measurements. From the N<sub>2</sub> absorption-desorption isotherms (Fig. 1e), these carbon aerogels can be seen to contain micropores (1.3 nm), mesopores (10 nm) and macropores (50 nm), as manifested in the corresponding pore size distributions (Fig. 1f). From the calculated BET specific surface areas in Table S2, it can be seen that the samples all show a hierarchical porous structure with a high surface area ranging from  $1542~\text{m}^2~\text{g}^{-1}$  for NCAG/Ru-1 to  $1359~\text{m}^2~\text{g}^{-1}$  for NCAG/Ru-2 and 1114 $\mbox{m}^2\,\mbox{g}^{-1}$  for NCAG/Ru-3, a unique feature conducive for the generation of single metal sites at the zigzag edges and nanowrinkles (vide infra). For comparison, the metal-free carbon aerogel (NCAG), which was prepared without the addition of Ru (but with the same content of PM as in NCAG/Ru-3), exhibited a surface area that was even 300 m<sup>2</sup> g<sup>-1</sup> greater than that of NCAG/Ru-3 (Table S2, Fig. S5). This suggests partial blocking of the nanopores by the metal species, in agreement with the increasing fraction of Ru single atoms from NCAG/Ru-1 to NCAG/Ru-3.

In XRD measurements (Fig. 1g), one can see that all samples exhibited two major diffractions peak at  $2\theta \approx 25^\circ$  and  $42^\circ$ , due to the carbon (002) and (101) facets (PDF card 65–6212), suggesting successful transformation of the biomass hydrogels to carbon aerogels. Additionally, no patterns of metal or metal oxide species can be resolved in the XRD patterns, most likely because of the minute metal contents

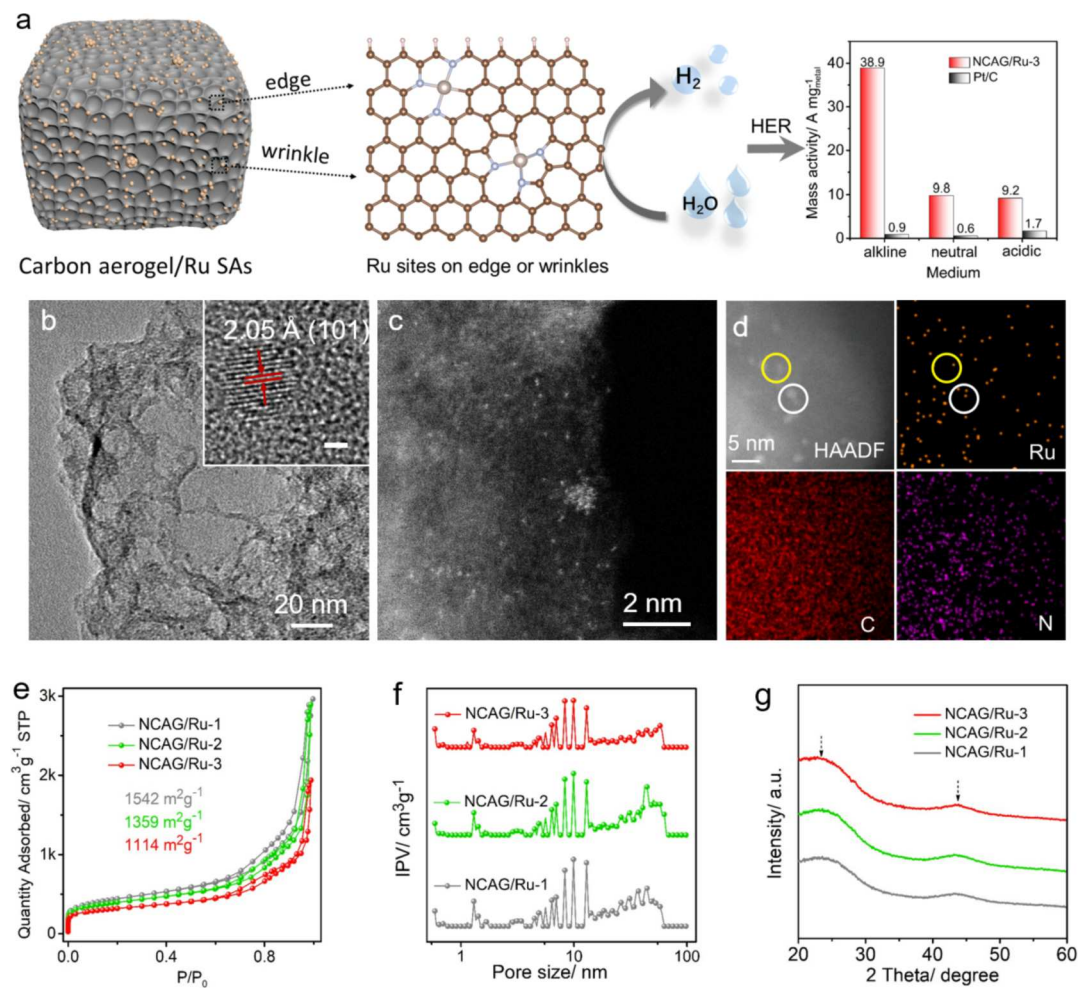


Fig. 1. (a) Schematic diagram of the Ru sites in carbon aerogel as the pH-universal HER catalysts. (b) TEM image of NCAG/Ru-3. Inset is the HRTEM image of a metal nanoparticle (scale bar 1 nm). (c) HAADF-STEM image and (d) the corresponding elemental maps of NCAG/Ru-3. (e) Nitrogen sorption isotherms, (f) pore size distribution, and (g) XRD patterns of NCAG/Ru-1, NCAG/Ru-2 and NCAG/Ru-3.

and small size of nanoclusters in the samples, in line with results from STEM measurements.

The chemical compositions and valency of the carbon aerogels were then assessed by X-ray photoelectron spectroscopy (XPS) measurements. One can see from the survey spectra (Fig. S6) that all samples contain only C, Ru, N, and O; and on the basis of the integrated peak areas, the carbon aerogels actually possess a similar elemental composition, ca. 88 wt% C, 8 wt% O, 4 wt% N, and 0.5 wt% Ru (Table S3). Notably, the Ru contents were consistent with the results from ICP-OES measurements (Table S1). The high-resolution scans of the Ru 3p electrons are depicted in Fig. 2a, where two doublets can be resolved at 261.8/284.2 eV and 263.8/286.1 eV, due to the  $3p_{3/2}/3p_{1/2}$  electrons of metallic Ru and Ru (II), respectively. This is in accord with the formation of Ru nanoclusters and atomically dispersed Ru in the carbon aerogels (Fig. 1). Furthermore, from Table S4, one can see that the fraction of Ru(II) increases in the order of NCAG/Ru-1 < NCAG/Ru-2 < NCAG/Ru-3, consistent with the increasing content of Ru single atom sites, as observed above. Similar results can be obtained from the high-resolution scans of Ru 3d electrons (Fig. S7). Fig. 2b shows the corresponding N 1 s spectra, where four kinds of N species can be resolved, pyridinic N, metal-N (M-N), pyridinic N, graphitic N, and oxidized N at 398.2, 399.0, 400.1, 401.0, and 403.0 eV, respectively. Notably, the percentages of both total N and Ru-N increase from NCAG/Ru-1 to NCAG/Ru-3 (Table S5). From the O 1 s spectra in Fig. 2c, one can see that C=O and C-O/O-H are the main O species in the samples, with only a negligible content of the metal-O species (Table S6). That is, results from the XPS studies indicate that the

carbon aerogels contained both Ru nanoclusters and  ${\rm RuN_x}$  moieties, and Ru single atom sites became increasingly dominant from NCAG/Ru-1 to NCAG/Ru-2 and to NCAG/Ru-3.

X-ray absorption spectroscopy (XAS) measurements were then performed to further examine the coordination configurations of the Ru sites in NCAG/Ru-3. From Fig. 2d, one can see that the K-edge profile of the X-ray absorption near-edge structure (XANES) of NCAG/Ru-3 is between those of Ru foil and RuO2, indicating that the average Ru valence state falls between 0 and +4, consistent with the formation of Ru single atom sites and Ru nanoclusters in the sample, as suggested in the above TEM and XPS measurements. The pre-edge peak at 22116 eV, which is due to the 1 s to 4pz shakedown transition of a square-planar configuration, shows only a weak intensity, suggesting the formation of a square-pyramidal or distorted octahedral configuration [52]. The corresponding R-space extended X-ray absorption fine structure (EXAFS) profiles are depicted in Fig. 2e. NCAG/Ru-3 can be seen to display two peaks at about 1.5 and 2.2 Å, due to the Ru-N and Ru-Ru shell, respectively. The strong Ru-N peak and much weaker Ru-Ru peak indicate that the atomically Ru sites are the major metal species in NCAG/Ru-3, in accord with results from XPS measurements. Additionally, fitting of the NCAG/Ru-3 EXAFS data (Fig. 2f and S8, Table S7) showed that the Ru-N path possessed a coordination number of ca. 5.2, implying that a square-pyramidal configuration is most likely for the Ru sites in NCAG/Ru-3.

On the ground of the above results, the configurations of the Ru atomic sites in NCAG/Ru-3 are constructed by the following steps. (i) As

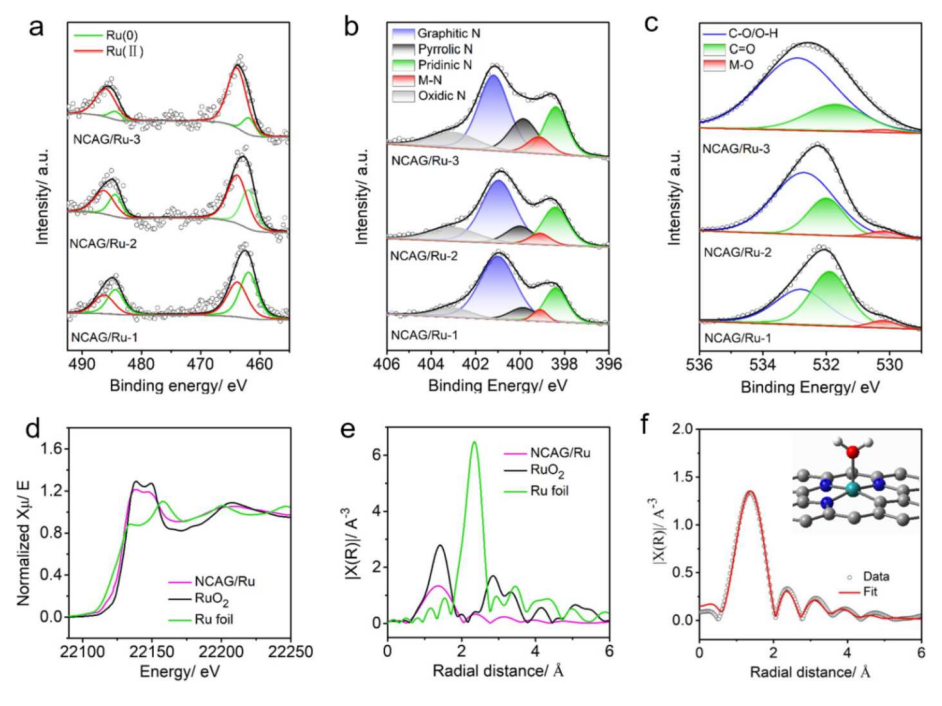


Fig. 2. High-resolution XPS scans of the (a) Ru 3p, (b) N 1 s and (c) O 1 s electrons of NCAG/Ru-1, NCAG/Ru-2 and NCAG/Ru-3. Symbols are experimental data and lines are deconvolution fits. (d) Ru K-edge spectra (XANES) and (e) R-space curves (EXAFS) of NCAG/Ru-3, RuO<sub>2</sub> and Ru foil. (f) EXAFS fitting of the NCAG/Ru-3 sample. Inset is a schematic of the RuN<sub>3</sub>C structure with the adsorption of one H<sub>2</sub>O molecule.

shown in Fig. 2e and S9, both the pre-edge and post-edge features of XANES can be seen to be consistent with those of RuN<sub>4</sub> with axial O ligands (RuN<sub>4</sub>–O) [52]. Because it is difficult to distinguish Ru–N and Ru–C by EXAFS due to their similar atomic mass, we proposed a RuN<sub>x</sub>C<sub>4-x</sub>–O site. (ii) The above XPS measurements confirmed that the Ru atoms were mainly chelated to N atoms, indicating the formation of RuN<sub>4</sub>–O, RuN<sub>3</sub>C–O or RuN<sub>2</sub>C<sub>2</sub>–O moieties (Fig. S10). (iii) Considering the reducing atmosphere during pyrolysis, the O atoms in these models were most likely provided by –OH or absorbed H<sub>2</sub>O and O<sub>2</sub> molecules, and the respective structure was denoted as RuN<sub>x</sub>C<sub>4-x</sub>–OH, RuN<sub>x</sub>C<sub>4-x</sub>–H<sub>2</sub>O, and RuN<sub>x</sub>C<sub>4-x</sub>–O<sub>2</sub> ( $x \ge 2$ ).

#### 3.2. HER electrocatalysis

Motivated by the unique structure of porous carbon aerogels embedded with atomically dispersed ruthenium, the electrocatalytic performance for HER was first investigated in 1.0 M KOH. From the linear sweep voltammograms (LSV) in Fig. 3a, all three carbon aerogels can be seen to exhibit apparent HER activity, which varied among the sample series. Specifically, to reach the current density of 10 mA cm $^{-2}$ , the NCAG/Ru-1 aerogel needed an overpotential ( $\eta_{10}$ ) of -104 mV, which was markedly reduced to -40 mV for NCAG/Ru-2, and only -4 mV for NCAG/Ru-3, in comparison to -58 mV for commercial 20 wt% Pt/C. The dramatically enhanced activity from NCAG/Ru-1 to NCAG/Ru-3 signifies the increasingly dominant contributions of the Ru single atom sites to the HER activity, as compared to the Ru nanoclusters [42,53]. The performance of NCAG/Ru-3 even surpassed relevant Ru-based catalysts recently reported in the literature (Table 1 and Fig. 3b).

NCAG/Ru-3 also possessed a lower Tafel slope (43.6 mV dec<sup>-1</sup>, Fig. 3c) than Pt/C (53.7 mV dec<sup>-1</sup>), NCAG/Ru-2 (56.7 mV dec<sup>-1</sup>) and NCAG/Ru-1 (107.2 mV dec<sup>-1</sup>). This implies enhanced HER kinetics on NCAG/Ru-3 in alkaline media. In fact, electrochemical impedance spectroscopy measurements (Fig. S11) showed that at the overpotential of –50 mV, the charge-transfer resistance ( $R_{ct}$ ) was the lowest at 43.6  $\Omega$  for NCAG/Ru-3, in comparison to 67.3  $\Omega$  for NCAG/Ru-2 and 198.9  $\Omega$  for NCAG/Ru-1, in good agreement with the remarkable HER activity of NCAG/Ru-3.

To differentiate the contributions of Ru single atoms and Ru nanoclusters to the HER activity, ethylenediaminetetraacetic acid (EDTA) and KSCN were used as poisoning species to inactivate the metal active sites. The shift of the  $\eta_{10}$  was denoted as  $\Delta E_1$  and  $\Delta E_2$  with the addition of 10 mM EDTA and 10 mM KSCN into 1.0 M KOH, respectively (Fig. 3d and S12); and  $\Delta E_3$  is defined as the difference between  $\Delta E_1$  and  $\Delta E_2$ . It is well known that EDTA predominantly coordinates with the RuN<sub>x</sub> sites, whereas SCN readily adsorbs onto both Ru nanocluster surfaces and  $RuN_x$  sites [42]. Thus,  $\Delta E_1$  and  $\Delta E_3$  were used to differentiate the contributions of the RuN<sub>x</sub> sites and Ru nanoclusters to HER. The percentage of  $\Delta E_1$  (or  $\Delta E_3$ ) to total contribution ( $\Delta E_1 + \Delta E_3$ ) for each catalyst is depicted in Fig. 3e, where the estimated contribution of RuN<sub>r</sub> sites to HER is 5%, 38% and 81% for NCAG/Ru-1, NCAG/Ru-2 and NCAG/Ru-3, respectively. This further confirms that the HER activity of NCAG/Ru-3 indeed arose predominantly from Ru single atom sites rather than Ru nanoclusters. That is, NCAG/Ru-3 exhibited the best HER activity among the series (which possessed a similar total Ru content, Table S1), because of the highest fraction of Ru single atoms (Fig. 2a).

The NCAG/Ru-3 nanocomposite also displayed remarkable HER activity in neutral and acidic media. As shown in Fig. 3f and S13, NCAG/Ru-3 exhibited an excellent HER performance in 1.0 M PBS with  $\eta_{10}=$  -45 mV and a Tafel slope of 96.1 mV dec $^{-1}$ , which is 38 mV and 17.1 mV dec $^{-1}$  lower than those of Pt/C. In 0.5 M H $_2$ SO $_4$  (Fig. 3g and S14), NCAG/Ru-3 displayed an  $\eta_{10}$  of -65 mV and a Tafel slope of 68.8 mV dec $^{-1}$ , somewhat higher than those of Pt/C (–32 mV, 40.5 mV dec $^{-1}$ ). Apparently, NCAG/Ru-3 shows more favorable HER activity and kinetics than commercial Pt/C in both neutral and alkaline media; and in the acidic media, the HER performance of NCAG/Ru-3 was somewhat subpar (Fig. 3h).

In fact, the NCAG/Ru-3 sample featured an ultrahigh mass activity of  $38.1 \, A \, mg_{Ru}^{-1}$  at  $-100 \, mV$  in alkaline media, 44 times better than that of Pt/C (Fig. 3i and S15), and in neutral and acidic media, the mass activity of NCAG/Ru-3 reached 9.2 and 10.1 A  $mg_{Ru}^{-1}$  at  $-100 \, mV$ , 16 and 6 times better than those of Pt/C, respectively (Fig. 3i and S16). The ultrahigh mass activity makes it possible to lower the cost of catalysts by reducing the consumption of precious metals. The remarkable pH-universal HER performance and extremely low metal content confirm

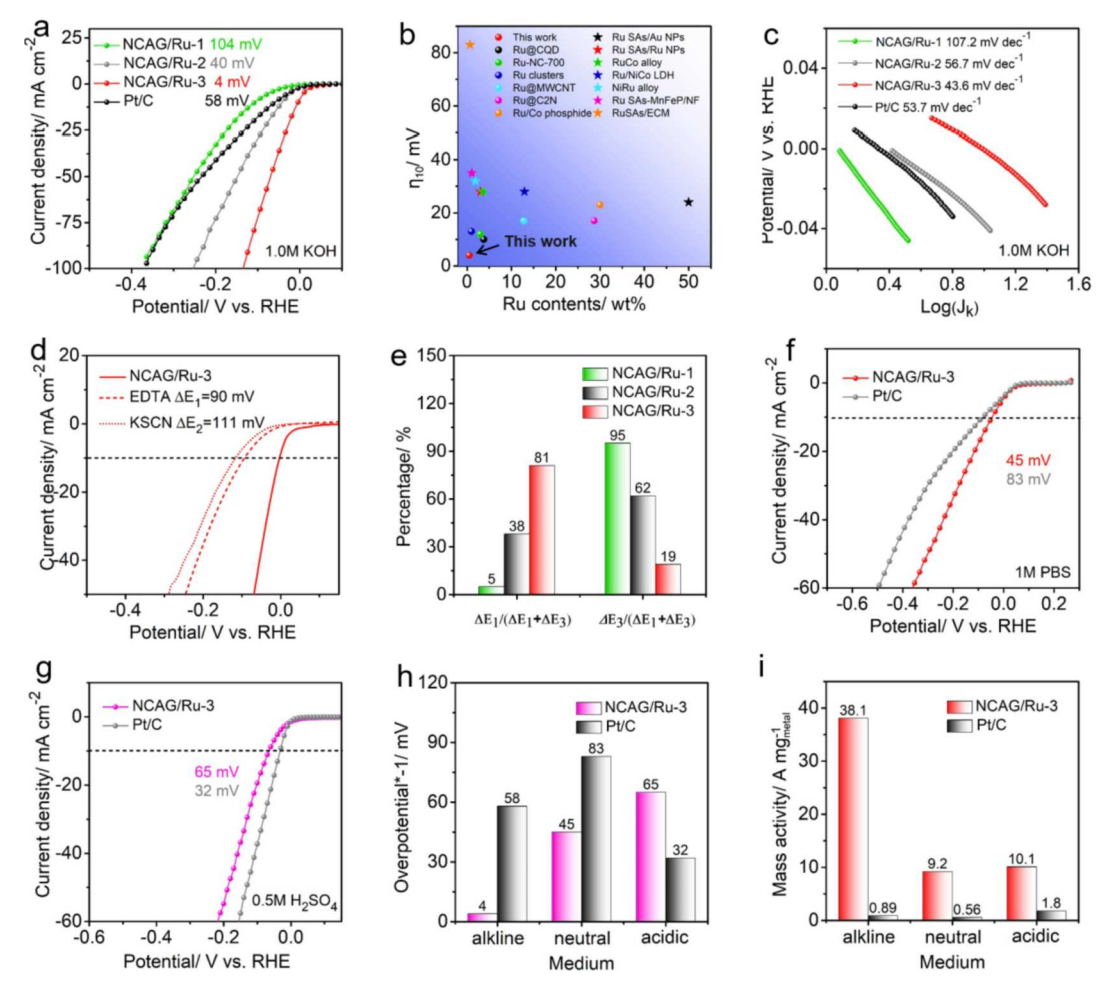


Fig. 3. (a) HER polarization curves in 1.0 M KOH of the NCAG/Ru carbon aerogels and commercial Pt/C. (b) Recently reported Ru-based catalysts and their metal content, HER activity in 1.0 M KOH. (c) Tafel plots obtained from the HER polarization curves in (a). (d) HER polarization curves of NCAG/Ru-3 in 1.0 M KOH in the absence and presence of 10 mM EDTA or 10 mM KSCN. (e) Percentage of  $\Delta E_1$  (or  $\Delta E_3$ ) to total contribution ( $\Delta E_1 + \Delta E_3$ ) for each catalyst. HER polarization curves in (f) 1.0 M phosphate buffer solution (PBS) and (g) 0.5 M  $H_2SO_4$  of the NCAG/Ru-3 and commercial Pt/C. (h) Overpotentials of NCAG/Ru-3 and Pt/C in different electrolyte media. (i) Mass activities of NCAG/Ru-3 and commercial Pt/C in 1.0 M KOH, 1.0 M PBS and 0.5 M  $H_2SO_4$  at the overpotential of -100 mV.

**Table 1**Comparison of HER performances of Ru-based catalysts.

Materials	Ru contents (wt%)	η <sub>10</sub> (mV)	Ref.
Ru SAs/carbon aerogel	0.47	-4	This work
Ru@CQD	3.78	-10	[54]
Ru-NC-700	3.0	-12	[42]
Ru clusters	1.0	-13	[19]
Ru@MWCNT	12.8	-17	[55]
Ru@C <sub>2</sub> N	28.7	-17	[20]
Ru cluster/Co phosphide	~30	-23	[56]
Ru SAs /Au NPs	>50	-24	[21]
Ru SAs/Ru PNs	3.04	-28	[57]
RuCo alloy	3.58	-28	[23]
Ru cluster/ NiCo LDH	12.95	-28	[58]
NiRu alloy	1.86	-32	[22]
Ru SAs-MnFeP/NF	1.08	-35	[59]
Ru SAs/ECM	0.68	-83	[53]

the optimal integration of highly active single Ru sites and porous 3D carbon aerogels in NCAG/Ru-3.

#### 3.3. Theoretical studies

Most Ru-based catalysts show excellent HER activity in alkaline media and outperform commercial Pt/C [19,20,60,61]. In alkaline HER,

the energy barrier for H2O dissociation serves as a critical variable to evaluate the electrocatalytic activity. Structural characterizations presented above (Fig. 2) showed that the most possible configurations of single Ru active sites were RuNxC4-x-OH, RuNxC4-x-H2O, and RuN- $_{x}C_{4-x}-O_{2}$  ( $x \ge 2$ ). Theoretical calculations indicate that it is difficult for RuN<sub>x</sub>C<sub>4-x</sub>-OH and RuN<sub>x</sub>C<sub>4-x</sub>-O<sub>2</sub> to adsorb H<sub>2</sub>O molecules, let alone H<sub>2</sub>O dissociation; and RuN<sub>x</sub>C<sub>4-x</sub>-H<sub>2</sub>O is the most possible Ru site in NCAG/ Ru-3 ( $x \ge 2$ , Fig. S17). The free energy of  $H_2O$  adsorption ( $\Delta G_{H2O^*}$ ) on RuN<sub>x</sub>C<sub>4-x</sub> was firstly calculated to further assess these structures. As show in Fig. S18, RuN<sub>4</sub> exhibits weak adsorption of H<sub>2</sub>O with a positive ΔG<sub>H2O\*</sub> of 0.03 eV, implying an unfavorable 5-coordination configuration. However, RuN<sub>3</sub>C and RuN<sub>2</sub>C<sub>2</sub> exhibit a negative  $\Delta G_{H2O^*}$  of -0.53eV and -0.39 eV, respectively, where the stronger H<sub>2</sub>O adsorption can lead to a stable 5-coordination configuration, consistent with results from the above XAS measurements. However, RuN<sub>2</sub>C<sub>2</sub> can be excluded by the much higher energy barrier towards H<sub>2</sub>O dissociation than that of RuN<sub>3</sub>C (Fig. S19). This indicates that the most probably active sites in this carbon aerogel are the H<sub>2</sub>O-adsorbed RuN<sub>3</sub>C moieties (Fig. 2f inset).

Generally, carbon aerogels exhibit two main features, rich pores and abundant nanowrinkles, which can result in the formation of edged metal sites and Stone-Wale defected metal sites [44]. Thus, three RuN<sub>3</sub>C structures in different positions of the graphited carbon are examined, normal RuN<sub>3</sub>C in the basal plane (RuN<sub>3</sub>C), RuN<sub>3</sub>C at the zigzag edge (RuN<sub>3</sub>C-ZZ), and RuN<sub>3</sub>C at the nanowrinkle (RuN<sub>3</sub>C-SW), which are highlighted in the HAADF-STEM image (Figure S20). As shown in

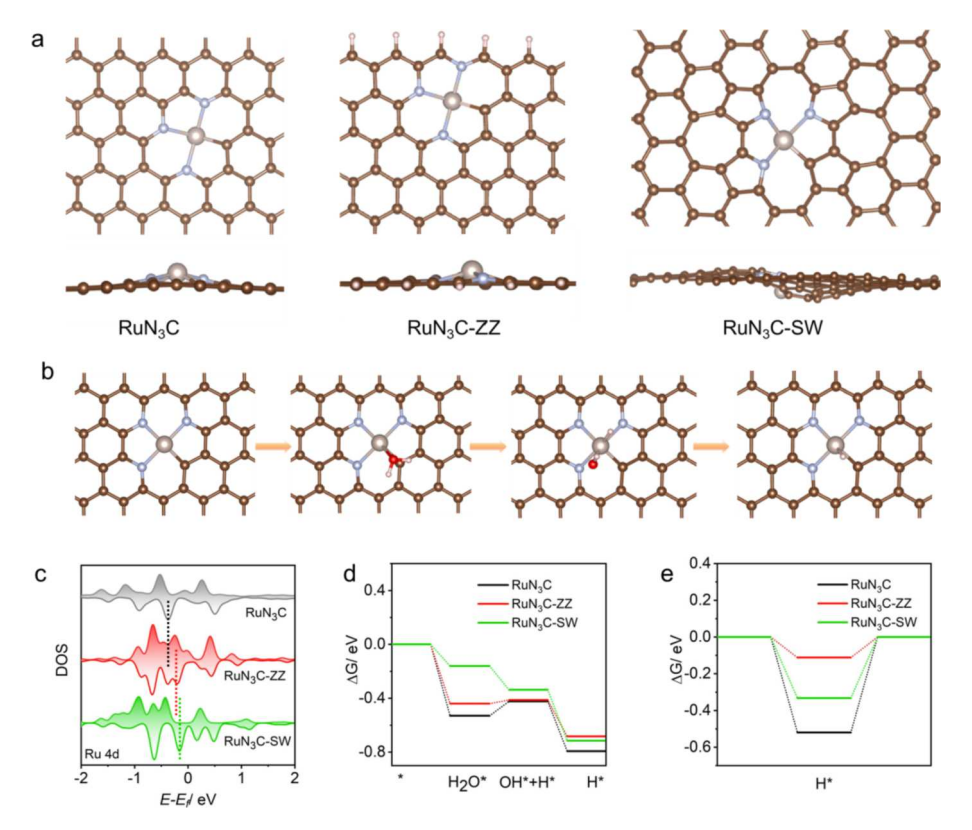


Fig. 4. (a) Top and side views of normal  $RuN_3C$  in the plane  $(RuN_3C)$ ,  $RuN_3C$  at the zigzag edge  $(RuN_3C-ZZ)$ , and  $RuN_3C$  at the nanowrinkle  $(RuN_3C-SW)$ . (b) Reaction pathway of  $H_2O$  absorption and dissociation on  $RuN_3C$ . (c) DOS of Ru 4d electrons, (d) Free energy diagram of  $H_2O$  dissociation on  $RuN_3C$ ,  $RuN_3C-ZZ$  and  $RuN_3C-SW$ . (e) H absorption/desorption energy of second H on  $RuN_3C$ ,  $RuN_3C-ZZ$  and  $RuN_3C-SW$ .

Fig. 4a, RuN<sub>3</sub>C and RuN<sub>3</sub>C-ZZ show a plane-like configuration where the Ru atoms were slightly extruded from the plane, while RuN<sub>3</sub>C-SW shows a distorted non-planar configuration with 5757 defects [62]. Fig. 4c and S21 display the total and Ru (4d) density of states (DOS) of RuN<sub>3</sub>C, RuN<sub>3</sub>C-ZZ and RuN<sub>3</sub>C-SW. In these configurations, the DOS near the Fermi level is mainly contributed by the Ru center (marked by the dotted lines in Fig. 4c and S21), implying that the Ru atom is the dominant active site. Apparently, the marked states of RuN<sub>3</sub>C-SW and RuN<sub>3</sub>C-ZZ are drastically closer to the Fermi level than those of RuN<sub>3</sub>C, suggesting a greater likelihood of electron donation and H<sub>2</sub>O activation.

Previous studies have shown that the rate-determining step (RDS) in alkaline HER is  $\rm H_2O$  dissociation (Volmer reaction) [34,42]. The reaction pathways from  $\rm H_2O$  adsorption to  $\rm H_2O$  dissociation on the RuN\_3C, RuN\_3C-ZZ and RuN\_3C-SW sites are shown in Fig. 4b, S22 and S23, respectively. The calculated free energies are presented in Fig. 4d. The  $\rm H_2O$  molecules are adsorbed onto these sites by the binding interaction between Ru and O atoms, with a  $\Delta G_{\rm H2O^*}$  of -0.53, -0.44 and -0.16 eV, respectively. The reaction pathway of  $\rm H_2O$  dissociation includes two steps, the split of the H-OH bond and desorption of the OH group. The latter is exothermic on the three sites, so the split of the H-OH bond is the RDS, which features an energy barrier of 0.1 eV for RuN\_3C and 0.02 eV for RuN\_3C-ZZ, suggesting that the metal sites on the zigzag edge are actually favored in  $\rm H_2O$  dissociation. Notably, the energy barrier of the RDS decreased further to -0.18 eV for RuN\_3C-SW, indicating an even faster  $\rm H_2O$  dissociation reaction.

The free energy of H absorption/desorption reaction ( $\Delta G_{H^*}$ ) is another indicator of HER activity [63–65]. Fig. 4e and S24 display the free energy diagrams of the first and second H absorption/desorption on the three sites [66]. The related H-absorbed configurations are shown in Fig. S25-S27. For the second H absorption/desorption, the energy barrier is 0.52 eV for RuN<sub>3</sub>C, and becomes substantially reduced to 0.33 eV for RuN<sub>3</sub>C-SW and further to 0.11 eV for RuN<sub>3</sub>C-ZZ, indicating enhanced H absorption/desorption reaction kinetics on the RuN<sub>3</sub>C-ZZ and RuN<sub>3</sub>C-

SW configurations.

To sum up,  $RuN_3C$  at the edges or nanowrinkles of the carbon aerogels greatly facilitate  $H_2O$  dissociation and/or promote H absorption/desorption, a unique feature that is conducive to HER electrocatalysis, as manifested above in electrochemical tests. With such a high activity, it becomes attractive to apply the NCAG/Ru-3 catalysts for electrochemical water splitting.

#### 3.4. Overall water splitting

To evaluate the catalytic activity and stability in practical applications, a two-electrode water splitting cell was constructed by utilizing commercial  $RuO_2$  as the anode catalyst and NCAG/Ru-3 or Pt/C as the cathode catalyst. Fig. 5a depicts the LSVs of water electrolysis in the resultant NCAG/Ru-3//RuO $_2$  and Pt/C//RuO $_2$  cells (with Ni foams as the current collectors) in 1.0 M KOH. The former can be seen to possess a higher activity, which needed an applied voltage of only 1.485 V to reach the current density of 10 mA cm $^{-2}$ , than the latter (1.505 V). In fact, a large number of  $H_2$  and  $O_2$  bubbles were generated and evolved at the NCAG/Ru-3//RuO $_2$  electrode surfaces at the constant current density of 10 mA cm $^{-2}$  (Fig. 5g) or when the cell was powered with a 1.50 V lithium-ion battery (Fig. 5h).

The long-term stability of the carbon aerogels for electrochemical water splitting was then examined in a constant-current electrolysis test. Fig. 5b shows the voltage–time (E-t) curves at the constant current of 10 mA cm $^{-2}$ . After 60 h's continuous operation, the applied voltage of NCAG/Ru-3//RuO $_2$  and Pt/C//RuO $_2$  cells increased by 30 and 50 mV, respectively, which was mainly due to the instability of the RuO $_2$  anode (Fig. S28), as LSV measurements showed that the HER  $\eta_{10}$  shifted negligibly by only -1 mV for NCAG/Ru-3 and -6 mV for the Pt/C electrode (Fig. 5b inset). This suggests a remarkable stability of NCAG/Ru-3 in alkaline water splitting.

Overall water splitting in neutral and acidic media were also tested in

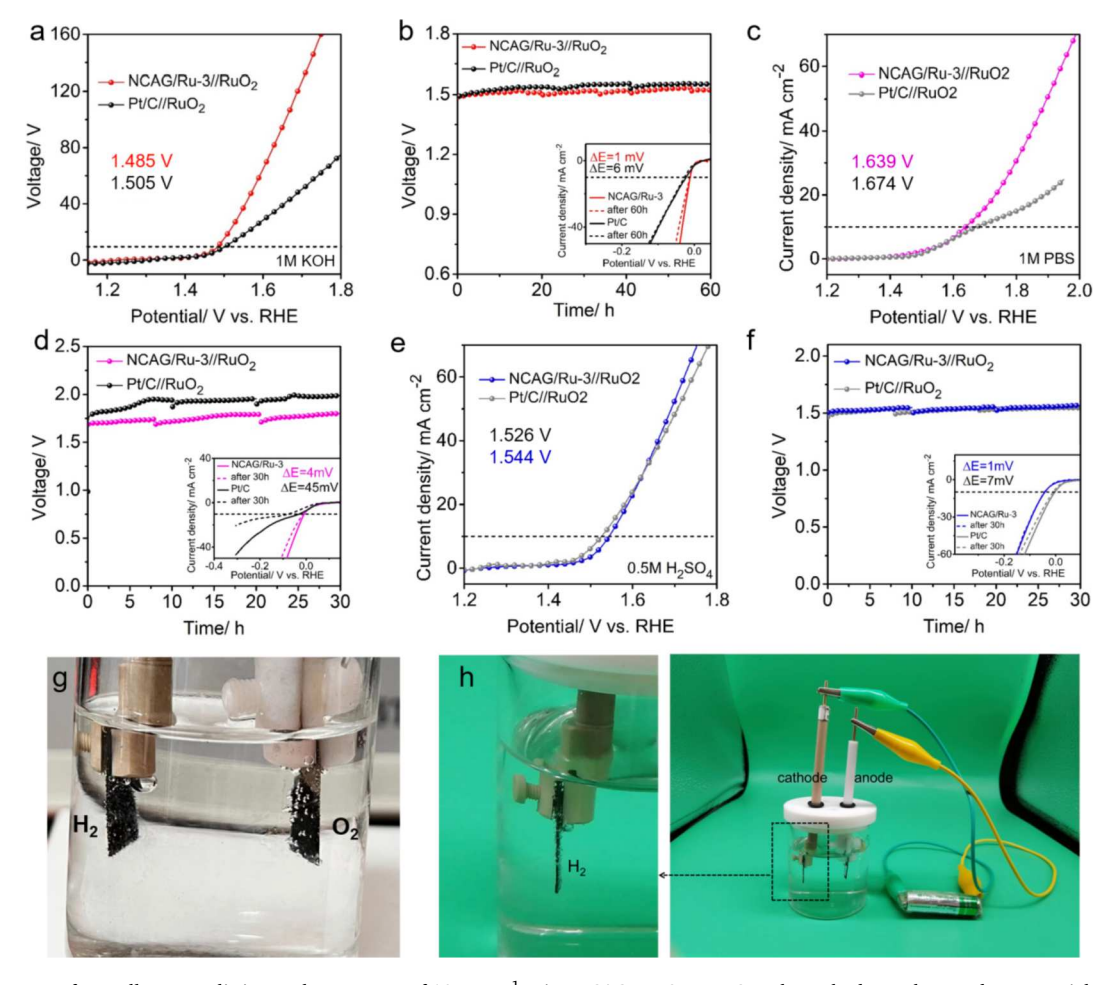


Fig. 5. (a) LSV curves of overall water splitting at the scan rate of  $10 \text{ mV s}^{-1}$  using NCAG/Ru-3 or Pt/C as the cathode catalyst, and commercial RuO<sub>2</sub> as the anode catalyst in 1.0 M KOH. (b) Constant-current electrolysis test at  $10 \text{ mA cm}^{-2}$  for 60 h in 1.0 M KOH. Inset shows the LSVs of NCAG/Ru-3 and Pt/C before and after constant-current electrolysis for 60 h. LSV curves of overall water splitting at the scan rate of  $10 \text{ mV s}^{-1}$  with NCAG/Ru-3 or Pt/C as the cathode catalyst and commercial RuO<sub>2</sub> as the anode catalyst in (c) 1.0 M PBS and (e) 0.5 M H<sub>2</sub>SO<sub>4</sub>. Constant-current electrolysis test for 30 h at  $10 \text{ mA cm}^{-2}$  in (d) 1.0 M PBS and (f) 0.5 M H<sub>2</sub>SO<sub>4</sub> (changing fresh electrolyte about every 10 h). The corresponding insets show the HER polarization curves of NCAG/Ru-3 and Pt/C before and after constant-current electrolysis for 30 h. (g) Photograph of water splitting by using the assembled NCAG/Ru-3//RuO<sub>2</sub> electrodes at a constant current of  $10 \text{ mA cm}^{-2}$ . (h) (right panel) Photograph of water splitting by the NCAG/Ru-3//RuO<sub>2</sub> cell powered by a 1.5 V lithium-ion battery in 1.0 KOH, and zoom in of the cathode in the left panel.

the same manner except that carbon paper was used as the current collector instead. As shown in Fig. 5c, to reach a water-splitting current density of 10 mA cm<sup>-2</sup>, the NCAG/Ru-3//RuO<sub>2</sub> cell required a potential bias of 1.639 V in 1.0 M PBS, 35 mV lower than that of Pt/C//RuO<sub>2</sub>. According to the constant-current E-t curves in electrolysis, the NCAG/ Ru-3 showed a more stable electrolytic potential than Pt/C (Fig. 5d). LSV studies indicate that the HER  $\eta_{10}$  of the NCAG/Ru-3 cathode exhibited a negative shift of only 4 mV, 40 mV less than that of Pt/C cathode after the electrolysis test for 30 h (Fig. 5d inset and Fig. S29a). For water splitting in 0.5 M H<sub>2</sub>SO<sub>4</sub>, both NCAG/Ru-3 and Pt/C show a remarkable activity with a low cell voltage of 1.544 and 1.526 V, as well as stable electrolytic potentials (Fig. 5e and 5f). After electrolysis test for 30 h, NCAG/Ru-3 and Pt/C cathode showed a 1 mV and 7 mV negative shift of the  $\eta_{10}$ , respectively, revealing excellent stability of NCAG/Ru-3 (Fig. 5f inset and Fig. S29b). These results confirm remarkable stability of NCAG/Ru-3 in pH-universal water splitting. Indeed, virtually no change was observed of the structural morphologies as well as Ru and N elemental contents and valence states of the NCAG/Ru-3 sample after the prolonged stability tests, as manifested in SEM and TEM (Fig. S30) and XPS measurements (Fig. S31, Table S8 and S9).

#### 4. Conclusions

In summary, carbon aerogels embedded with atomically dispersed Ru sites and Ru nanoclusters were prepared pyrolytically by using biomass hydrogels as precursors and structural templates, and exhibited ultrahigh mass activity and stability towards HER across a wide range of pH (0 to 14), as compared to commercial Pt/C. Notably, the HER activity increased markedly with an increasing fraction of the Ru single atom sites, and the best sample (NCAG/Ru-3) exhibited an  $\eta_{10}$  of only  $-4\ mV$ and a mass activity of 38.1 A mg<sub>Ru</sub>-1 in 1.0 M KOH, markedly outperforming commercial Pt/C benchmark and relevant Ru-derived catalysts reported recently in the literature. With NCAG/Ru-3 as the cathode catalyst and commercial RuO2 as the anode catalyst for overall water splitting, the cell showed comparable or even better activity and stability than that built upon commercial Pt/C//RuO<sub>2</sub> in such a wide pH range. DFT calculations showed that the excellent pH-universal HER activity was attributed to the high intrinsic activity of the RuN<sub>r</sub> sites at the edges and nanowrinkles of the porous carbon aerogels that facilitated water adsorption and dissociation in alkaline and neutral media and hydrogen adsorption in acidic media. Results from this study may open a new avenue in the rational design and engineering of highefficiency, low-cost HER catalysts based on carbon aerogel-supported single metal atoms for pH-universal water splitting.

#### CRediT authorship contribution statement

Ting He: Conceptualization, Investigation, Writing – original draft. Yaya Song: Visualization, Investigation, Resources. Yang Chen: Visualization, Investigation, Resources. Xianwen Song: Data curation, Software. Bingzhang Lu: Validation, Software. Qiming Liu: Validation, Software. Hongtao Liu: Funding acquisition. Yi Zhang: Supervision, Funding acquisition, Writing – review & editing. Xiaoping Ouyang: Supervision, Funding acquisition, Writing – review & editing. Shaowei Chen: Supervision, Funding acquisition, Writing – review & editing.

#### **Declaration of Competing Interest**

The authors declare that they have no known competing financial interests or personal relationships that could have appeared to influence the work reported in this paper.

#### Acknowledgments

H. T. L. acknowledges the National Key R&D Program of China (No. 2019YFA0210300). Y. Z. acknowledges support from the National Natural Science Foundation of China (21972169, 21773311) and Hunan Provincial Science and Technology Plan Project (2017TP1001). T. H. thanks the Postdoctoral Research Foundation of Central South University (140050038). Y. S. was supported by the Fundamental Research Funds for the Central Universities of Central South University (1053320210029). S. W. C. acknowledges support from the National Science Foundation (CHE-2003685 and CHE-1900235). Computational studies were conducted at Eceshi (www.eceshi.com) and the High-Performance Computing Center of Central South University.

#### Appendix A. Supplementary data

Supplementary data to this article can be found online at https://doi.org/10.1016/j.cej.2022.136337.

#### References

- [1] Y. Qu, B. Chen, Z. Li, X. Duan, L. Wang, Y. Lin, T. Yuan, F. Zhou, Y. Hu, Z. Yang, C. Zhao, J. Wang, C. Zhao, Y. Hu, G. Wu, Q. Zhang, Q. Xu, B. Liu, P. Gao, R. You, W. Huang, L. Zheng, L. Gu, Y. Wu, Y. Li, Thermal emitting strategy to synthesize atomically dispersed Pt metal sites from bulk Pt metal, J. Am. Chem. Soc. 141 (11) (2019) 4505–4509.
- [2] P. Kuang, Y. Wang, B. Zhu, F. Xia, C.-W. Tung, J. Wu, H.M. Chen, J. Yu, Pt Single atoms supported on N-Doped mesoporous hollow carbon spheres with enhanced electrocatalytic H<sub>2</sub>-evolution activity, Adv. Mater. 33 (18) (2021) 2008599.
- [3] C. Lin, Z. Huang, Z. Zhang, T. Zeng, R. Chen, Y. Tan, W. Wu, S. Mu, N. Cheng, Structurally ordered Pt<sub>3</sub>Co nanoparticles anchored on N-doped graphene for highly efficient hydrogen evolution reaction, ACS Sustain. Chem. Eng. 8 (45) (2020) 16938–16945.
- [4] C. Fan, X. Jiang, J. Chen, X.u. Wang, S. Qian, C. Zhao, L. Ding, D. Sun, Y. Tang, Low-Load Pt Nanoclusters Anchored on Graphene Hollow Spheres for Efficient Hydrogen Evolution, Small Struct. 2 (1) (2021) 2000017.
- [5] S.L. Zhang, X.F. Lu, Z.-P. Wu, D. Luan, X.W.(. Lou, Engineering Platinum-Cobalt Nano-alloys in Porous Nitrogen-Doped Carbon Nanotubes for Highly Efficient Electrocatalytic Hydrogen Evolution, Angew. Chem. Int. Ed. 60 (35) (2021) 19068–19073
- [6] X.-K. Wan, H.B. Wu, B.Y. Guan, D. Luan, X.W.(. Lou, Confining Sub-Nanometer Pt Clusters in Hollow Mesoporous Carbon Spheres for Boosting Hydrogen Evolution Activity, Adv. Mater. 32 (7) (2020) 1901349.
- [7] J. Qian, S. Li, Q. Liu, R. Ma, S. Li, J. Wang, Incomplete amorphous phosphorization on the surface of crystalline cobalt molybdate to accelerate hydrogen evolution, J. Mater. Chem. A 9 (38) (2021) 21859–21866.
- [8] W. Wang, L. Yang, J. Chen, S. Wu, M. Chen, X. Liang, D. Zhou, C. Liu, Realizing electronic modulation on Mo sites for efficient hydrogen evolution reaction, J. Mater. Chem. A 8 (35) (2020) 18180–18187.
- [9] T. He, Y.i. Peng, Q. Li, J.E. Lu, Q. Liu, R. Mercado, Y. Chen, F. Nichols, Y.i. Zhang, S. Chen, Nanocomposites Based on Ruthenium Nanoparticles Supported on Cobalt and Nitrogen-Codoped Graphene Nanosheets as Bifunctional Catalysts for Electrochemical Water Splitting, ACS Appl. Mater. Interfaces 11 (50) (2019) 46912–46919.
- [10] Z.-L. Wang, K. Sun, J. Henzie, X. Hao, C. Li, T. Takei, Y.-M. Kang, Y. Yamauchi, Spatially Confined Assembly of Monodisperse Ruthenium Nanoclusters in a

- Hierarchically Ordered Carbon Electrode for Efficient Hydrogen Evolution, Angew. Chem. Int. Ed. 57 (20) (2018) 5848–5852.
- [11] P. Su, W. Pei, X. Wang, Y. Ma, Q. Jiang, J. Liang, S. Zhou, J. Zhao, J. Liu, G.Q. Lu, Exceptional electrochemical HER performance with enhanced electron transfer between Ru nanoparticles and single atoms dispersed on carbon substrate, Angew. Chem. Int. Ed. 60 (2021) 16044–16050.
- [12] Y.Y. Zhang, N. Zhang, P. Peng, W. Rui, Y. Jin, Y.K. Lv, X. Wang, W. Wei, S.Q. Zang, Uniformly Dispersed Ru Nanoparticles Constructed by In Situ Confined Polymerization of Ionic Liquids for the Electrocatalytic Hydrogen Evolution Reaction, Small Methods 5 (2021) 2100505.
- [13] W. Li, Y. Zhao, Y. Liu, M. Sun, G.I.N. Waterhouse, B. Huang, K. Zhang, T. Zhang, S. Lu, Exploiting Ru-induced Lattice Strain in CoRu Nanoalloys for Robust Bifunctional Hydrogen Production, Angew. Chem. Int. Ed. 60 (2020) 3290–3298.
- [14] Q. Xie, Z. Wang, L. Lin, Y. Shu, J. Zhang, C. Li, Y. Shen, H. Uyama, Nanoscaled and Atomic Ruthenium Electrocatalysts Confined Inside Super-Hydrophilic Carbon Nanofibers for Efficient Hydrogen Evolution Reaction, Small 17 (2021) 2102160.
- [15] H. Zhang, Y. Lv, C. Chen, C. Lv, X. Wu, J. Guo, D. Jia, Inter-doped ruthenium-nickel oxide heterostructure nanosheets with dual active centers for electrochemical-/solar-driven overall water splitting, Appl. Catal., B 298 (2021), 120611
- [16] B. Yang, J. Xu, D. Bin, J. Wang, J. Zhao, Y. Liu, B. Li, X. Fang, Y. Liu, L. Qiao, L. Liu, B. Liu, Amorphous phosphatized ruthenium-iron bimetallic nanoclusters with Ptlike activity for hydrogen evolution reaction, Appl. Catal., B 283 (2021), 119583.
- [17] T. Wu, J. Hong, Z. Lu, H. Wu, C. Wu, Z. Tang, X. Liu, B. Zeng, Y. Xu, G. Chen, C. Yuan, L. Dai, In-situ generation of Ru-catechol coordinative polymer precursor for high-performance hydrogen evolution reaction doped carbon catalyst, Appl. Catal., B 285 (2021), 119795.
- [18] J. Wang, W. Fang, Y. Hu, Y. Zhang, J. Dang, Y. Wu, B. Chen, H. Zhao, Z. Li, Single atom Ru doping 2H-MoS<sub>2</sub> as highly efficient hydrogen evolution reaction electrocatalyst in a wide pH range, Appl. Catal., B 298 (2021), 120490.
- [19] Y.L. Wu, X.F. Li, Y.S. Wei, Z.M. Fu, W.B. Wei, X.T. Wu, Q.L. Zhu, Q. Xu, Ordered Macroporous Superstructure of Nitrogen-Doped Nanoporous Carbon Implanted with Ultrafine Ru Nanoclusters for Efficient pH-Universal Hydrogen Evolution Reaction, Adv. Mater. 33 (2021) 2006965.
- [20] J. Mahmood, F. Li, S.-M. Jung, M.S. Okyay, I. Ahmad, S.-J. Kim, N. Park, H. Y. Jeong, J.-B. Baek, An Efficient and pH-Universal Ruthenium-Based Catalyst for the Hydrogen Evolution Reaction, Nat. Nanotechnol. 12 (2017) 441–447.
- [21] C.-H. Chen, D. Wu, Z. Li, R. Zhang, C.-G. Kuai, X.-R. Zhao, C.-K. Dong, S.-Z. Qiao, H. Liu, X.-W. Du, Ruthenium-Based Single-Atom Alloy with High Electrocatalytic Activity for Hydrogen Evolution, Adv. Energy Mater. 9 (20) (2019) 1803913.
- [22] Y. Xu, S. Yin, C. Li, K. Deng, H. Xue, X. Li, H. Wang, L. Wang, Low-Ruthenium-Content NiRu Nanoalloys Encapsulated in Nitrogen-Doped Carbon as Highly Efficient and pH-Universal Electrocatalysts for the Hydrogen Evolution Reaction, J. Mater. Chem. A 6 (4) (2018) 1376–1381.
- [23] J. Su, Y. Yang, G. Xia, J. Chen, P. Jiang, Q. Chen, Ruthenium-cobalt nanoalloys encapsulated in nitrogen-doped graphene as active electrocatalysts for producing hydrogen in alkaline media, Nat. Commun. 8 (2017) 14969.
- [24] X. Mu, J. Gu, F. Feng, Z. Xiao, C. Chen, S. Liu, S. Mu, RuRh Bimetallene Nanoring as High-efficiency pH-Universal Catalyst for Hydrogen Evolution Reaction, Adv. Sci. 8 (2) (2021) 2002341.
- [25] Y.i. Peng, B. Lu, L. Chen, N. Wang, J.E. Lu, Y. Ping, S. Chen, Hydrogen Evolution Reaction Catalyzed by Ruthenium Ion-Complexed Graphitic Carbon Nitride Nanosheets, J. Mater. Chem. A 5 (34) (2017) 18261–18269.
- [26] Q. Song, X. Qiao, L. Liu, Z. Xue, C. Huang, T. Wang, Ruthenium@N-doped Graphite Carbon Derived from Carbon Foam for Efficient Hydrogen Evolution Reaction, Chem. Commun. 55 (2019) 965–968.
- [27] J.N. Tiwari, A.M. Harzandi, M. Ha, S. Sultan, C.W. Myung, H.J. Park, D.Y. Kim, P. Thangavel, A.N. Singh, P. Sharma, S.S. Chandrasekaran, F. Salehnia, J.-W. Jang, H.S. Shin, Z. Lee, K.S. Kim, High-Performance Hydrogen Evolution by Ru Single Atoms and Nitrided-Ru Nanoparticles Implanted on N-Doped Graphitic Sheet, Adv. Energy Mater. 9 (2019) 1900931.
- [28] C. Cai, K. Liu, Y. Zhu, P. Li, Q. Wang, B. Liu, S. Chen, H. Li, L. Zhu, H. Li, J. Fu, Y. Chen, E. Pensa, J. Hu, Y.-R. Lu, T.-S. Chan, E. Cortes, M. Liu, Optimizing hydrogen binding on Ru sites with RuCo alloy nanosheets for efficient alkaline hydrogen evolution, Angew. Chem. Int. Ed. 61 (2021), e2021136.
- [29] Y. Song, J. Cheng, J. Liu, Q. Ye, X. Gao, J. Lu, Y. Cheng, Modulating electronic structure of cobalt phosphide porous nanofiber by ruthenium and nickel dual doping for highly-efficiency overall water splitting at high current density, Appl. Catal., B 298 (2021), 120488.
- [30] A.M. Harzandi, S. Shadman, M. Ha, C.W. Myung, D.Y. Kim, H.J. Park, S. Sultan, W.-S. Noh, W. Lee, P. Thangavel, W.J. Byun, S.-H. Lee, J.N. Tiwari, T.J. Shin, J.-H. Park, Z. Lee, J.S. Lee, K.S. Kim, Immiscible bi-metal single-atoms driven synthesis of electrocatalysts having superb mass-activity and durability, Appl. Catal., B 270 (2020), 118896.
- [31] Y. Liu, X. Li, Q. Zhang, W. Li, Y. Xie, H. Liu, L. Shang, Z. Liu, Z. Chen, L. Gu, Z. Tang, T. Zhang, S. Lu, A General Route to Prepare Low-Ruthenium-Content Bimetallic Electrocatalysts for pH-Universal Hydrogen Evolution Reaction by Using Carbon Quantum Dots, Angew. Chem. Int. Ed. 59 (2020) 1718–1726.
- [32] Y.-H. Wang, R.-Q. Li, H.-B. Li, H.-L. Huang, Z.-J. Guo, H.-Y. Chen, Y. Zheng, K.-G. Qu, Controlled synthesis of ultrasmall RuP<sub>2</sub> particles on N, P-codoped carbon as superior pH-wide electrocatalyst for hydrogen evolution, Rare Met. 40 (2021) 1040–1047.
- [33] J. Yu, G. Li, H. Liu, L. Zhao, A. Wang, Z. Liu, H. Li, H. Liu, Y. Hu, W. Zhou, Ru–Ru2PΦNPC and NPC@RuO<sub>2</sub> Synthesized via Environment-Friendly and Solid-Phase Phosphating Process by Saccharomycetes as N/P Sources and Carbon

- Template for Overall Water Splitting in Acid Electrolyte, Adv. Funct. Mater. 29 (2019) 1901154.
- [34] S. Ye, F. Luo, T. Xu, P. Zhang, H. Shi, S. Qin, J. Wu, C. He, X. Ouyang, Q. Zhang, J. Liu, X. Sun, Boosting the alkaline hydrogen evolution of Ru nanoclusters anchored on B/N-doped graphene by accelerating water dissociation, Nano Energy 68 (2020), 104301.
- [35] M. Lao, G. Zhao, P. Li, T. Ma, Y. Jiang, H. Pan, S.X. Dou, W. Sun, Manipulating the Coordination Chemistry of RuN(O)C Moieties for Fast Alkaline Hydrogen Evolution Kinetics, Adv. Funct. Mater. 31 (2021) 2100698.
- [36] P. Li, X. Duan, S. Wang, L. Zheng, Y. Li, H. Duan, Y. Kuang, X. Sun, Amorphous Ruthenium-Sulfide with Isolated Catalytic Sites for Pt-Like Electrocatalytic Hydrogen Production Over Whole pH Range, Small 15 (46) (2019) 1904043.
- [37] Z. Chen, J. Lu, Y. Ai, Y. Ji, T. Adschiri, L. Wan, Ruthenium/Graphene-like Layered Carbon Composite as an Efficient Hydrogen Evolution Reaction Electrocatalyst, ACS Appl. Mater. Interfaces 8 (51) (2016) 35132–35137.
- [38] J.-Q. Chi, W.-K. Gao, J.-H. Lin, B. Dong, K.-L. Yan, J.-F. Qin, B. Liu, Y.-M. Chai, C.-G. Liu, Hydrogen Evolution Activity of Ruthenium Phosphides Encapsulated in Nitrogen- and Phosphorous-Codoped Hollow Carbon Nanospheres, ChemSusChem 11 (4) (2018) 743–752.
- [39] L. Yang, M.B. Vukmirovic, D. Su, K. Sasaki, J.A. Herron, M. Mavrikakis, S. Liao, R. R. Adzic, Tuning the Catalytic Activity of Ru@Pt Core-Shell Nanoparticles for the Oxygen Reduction Reaction by Varying the Shell Thickness, J. Phys. Chem. C 117 (4) (2013) 1748–1753.
- [40] Y. Zheng, Y. Jiao, Y. Zhu, L.H. Li, Y.u. Han, Y. Chen, M. Jaroniec, S.-Z. Qiao, High Electrocatalytic Hydrogen Evolution Activity of an Anomalous Ruthenium Catalyst, J. Am. Chem. Soc. 138 (49) (2016) 16174–16181.
- [41] Y. Lee, J.H. Ahn, S. Shin, S.-H. Jung, H.-S. Park, Y.-G. Cho, D.-G. Lee, H. Kong, J. H. Lee, H.-K. Song, Metal-nitrogen intimacy of the nitrogen-doped ruthenium oxide for facilitating electrochemical hydrogen production, Appl. Catal., B 303 (2022) 120873
- [42] B. Lu, L. Guo, F. Wu, Y. Peng, J.E. Lu, T.J. Smart, N. Wang, Y.Z. Finfrock, D. Morris, P. Zhang, N. Li, P. Gao, Y. Ping, S. Chen, Ruthenium Atomically Dispersed in Carbon Outperforms Platinum toward Hydrogen Evolution in Alkaline Media, Nat. Commun. 10 (2019) 631.
- [43] Y. Chen, S. Hu, F. Nichols, F. Bridges, S. Kan, T. He, Y.i. Zhang, S. Chen, Carbon aerogels with atomic dispersion of binary iron-cobalt sites as effective oxygen catalysts for flexible zinc-air batteries, J. Mater. Chem. A 8 (23) (2020) 11649–11655.
- [44] T. He, B. Lu, Y. Chen, Y. Wang, Y. Zhang, J.L. Davenport, A.P. Chen, C.-W. Pao, M. Liu, Z. Sun, Nanowrinkled Carbon Aerogels Embedded with FeN<sub>x</sub> Sites as Effective Oxygen Electrodes for Rechargeable Zinc-Air Battery, Research 2019 (2019) 6813585.
- [45] T. He, Y. Zhang, Y. Chen, Z. Zhang, H.-Y. Wang, Y. Hu, M. Liu, C.-W. Pao, J.-L. Chen, L.-Y. Chang, Z. Sun, J. Xiang, Y. Zhang, S. Chen, Single iron atoms stabilized by microporous defects of biomass-derived carbon aerogels as high-performance electrocatalysts for aluminium-air battery, J. Mater. Chem. A 7 (2019) 20840–20846.
- [46] B.J. Zhu, C. Qu, S. Gao, Z.B. Liang, H. Zhang, R.Q. Zou, Ultralow Loading Ruthenium Nanoparticles on Nitrogen-Doped Graphene Aerogel for Trifunctional Electrocatalysis, ChemCatChem 10 (2018) 1113–1121.
- [47] R. Jiang, L. Li, T. Sheng, G. Hu, Y. Chen, L. Wang, Edge-Site Engineering of Atomically Dispersed Fe-N<sub>4</sub> by Selective C-N Bond Cleavage for Enhanced Oxygen Reduction Reaction Activities, J. Am. Chem. Soc. 140 (2018) 11594–11598.
- [48] G. Kresse, J. Furthmüller, Efficient iterative schemes for ab initio total-energy calculations using a plane-wave basis set, Phys. Rev. B 54 (1996) 11169–11186.
- [49] P.E. Blöchl, Projector augmented-wave method, Phys. Rev. B 50 (1994) 17953–17979.
- [50] G. Kresse, D. Joubert, From ultrasoft pseudopotentials to the projector augmentedwave method, Phys. Rev. B 59 (1999) 1758–1775.

- [51] J.P. Perdew, J.A. Chevary, S.H. Vosko, K.A. Jackson, M.R. Pederson, D.J. Singh, C. Fiolhais, Atoms, molecules, solids, and surfaces: Applications of the generalized gradient approximation for exchange and correlation, Phys. Rev. B 46 (1992) 6671–6687
- [52] C. Zhang, J. Sha, H. Fei, M. Liu, S. Yazdi, J. Zhang, Q. Zhong, X. Zou, N. Zhao, H. Yu, Z. Jiang, E. Ringe, B.I. Yakobson, J. Dong, D. Chen, J.M. Tour, Single-Atomic Ruthenium Catalytic Sites on Nitrogen-Doped Graphene for Oxygen Reduction Reaction in Acidic Medium, ACS Nano 11 (2017) 6930–6941.
- [53] H.B. Zhang, W. Zhou, X.F. Lu, T. Chen, X.W. Lou, Implanting Isolated Ru Atoms into Edge-Rich Carbon Matrix for Efficient Electrocatalytic Hydrogen Evolution, Adv. Energy Mater. 10 (2020) 2000882.
- [54] W. Li, Y. Liu, M. Wu, X. Feng, S.A.T. Redfern, Y. Shang, X. Yong, T. Feng, K. Wu, Z. Liu, B. Li, Z. Chen, J.S. Tse, S. Lu, B. Yang, Carbon-Quantum-Dots-Loaded Ruthenium Nanoparticles as an Efficient Electrocatalyst for Hydrogen Production in Alkaline Media, Adv. Mater. 30 (2018) 1800676.
- [55] D.H. Kweon, M.S. Okyay, S.-J. Kim, J.-P. Jeon, H.-J. Noh, N. Park, J. Mahmood, J.-B. Baek, Ruthenium anchored on carbon nanotube electrocatalyst for hydrogen production with enhanced Faradaic efficiency, Nat. Commun. 11 (2020) 1278.
- [56] J. Xu, T. Liu, J. Li, B. Li, Y. Liu, B. Zhang, D. Xiong, I. Amorim, W. Li, L. Liu, Boosting the Hydrogen Evolution Performance of Ruthenium Clusters through Synergistic Coupling with Cobalt Phosphide, Energy Environ. Sci. 11 (2018) 1819–1827.
- [57] J. Peng, Y.H. Chen, K. Wang, Z.H. Tang, S.W. Chen, High-performance Ru-based electrocatalyst composed of Ru nanoparticles and Ru single atoms for hydrogen evolution reaction in alkaline solution, Int. J. Hydrogen Energy 45 (2020) 18840–18849.
- [58] D. Li, B.W. Zhang, Y. Li, R.S. Chen, S. Hu, H.W. Ni, Boosting hydrogen evolution activity in alkaline media with dispersed ruthenium clusters in NiCo-layered double hydroxide, Electrochem. Commun. 101 (2019) 23–27.
- [59] D. Chen, Z.H. Pu, R.H. Lu, P.X. Ji, P.Y. Wang, J.W. Zhu, C. Lin, H.W. Li, X.G. Zhou, Z.Y. Hu, F.J. Xia, J.S. Wu, S.C. Mu, Ultralow Ru Loading Transition Metal Phosphides as High-Efficient Bifunctional Electrocatalyst for a Solar-to-Hydrogen Generation System, Adv. Energy Mater. 10 (2020) 2000814.
- [60] C. Hu, E. Song, M. Wang, W. Chen, F. Huang, Z. Feng, J. Liu, J. Wang, Partial-Single-Atom, Partial-Nanoparticle Composites Enhance Water Dissociation for Hydrogen Evolution, Adv. Sci. 8 (2020) 2001881.
- [61] L. Zhang, H. Jang, Y. Wang, Z. Li, W. Zhang, M.G. Kim, D. Yang, S. Liu, X. Liu, J. Cho, Exploring the Dominant Role of Atomic- and Nano-Ruthenium as Active Sites for Hydrogen Evolution Reaction in Both Acidic and Alkaline Media, Adv. Sci. 8 (2021) 2004516.
- [62] K. Khan, X. Yan, Q. Yu, S.-H. Bae, J.J. White, J. Liu, T. Liu, C. Sun, J. Kim, H.-M. Cheng, Y. Wang, B. Liu, K. Amine, X. Pan, Z. Luo, Stone-Wales Defect-rich carbon-supported dual-metal single atom sites for Zn-air batteries, Nano Energy 90 (2021). 106488.
- [63] W. Xiao, L. Zhang, D. Bukhvalov, Z. Chen, Z. Zou, L. Shang, X. Yang, D. Yan, F. Han, T. Zhang, Hierarchical ultrathin carbon encapsulating transition metal doped MoP electrocatalysts for efficient and pH-universal hydrogen evolution reaction. Nano Energy 70 (2020), 104445.
- [64] W. Cheng, H. Zhang, D. Luan, X.W. Lou, Exposing unsaturated Cu<sub>1</sub>-O<sub>2</sub> sites sites in nanoscale Cu-MOF for efficient electrocatalytic hydrogen evolution, Sci. Adv., 7 (2021) eabg2580.
- [65] J. Cai, Y. Song, Y. Zang, S. Niu, Y. Wu, Y. Xie, X. Zheng, Y. Liu, Y. Lin, X. Liu, G. Wang, Y. Qian, N-induced lattice contraction generally boosts the hydrogen evolution catalysis of P-rich metal phosphides, Sci. Adv. 6 (2020) eaaw8113.
- [66] D. Liu, X. Li, S. Chen, H. Yan, C. Wang, C. Wu, Y.A. Haleem, S. Duan, J. Lu, B. Ge, P. M. Ajayan, Y.i. Luo, J. Jiang, L.i. Song, Atomically dispersed platinum supported on curved carbon supports for efficient electrocatalytic hydrogen evolution, Nat. Energy 4 (6) (2019) 512–518.